

Contacts to Low-Dimensional Semiconductors: Physical Theory and Analytical Model

Jimmy Qin* and H.-S. Philip Wong

Department of Electrical Engineering, Stanford University, Stanford, CA 94305, USA

Metal contacts to low-dimensional semiconductors are critical for nanoelectronics, yet a general physical description has remained elusive. We present an analytical model for metal-induced gap states (MIGS), revealing a universal scaling law governed by semiconductor dimensionality. Linking MIGS to transport observables, we provide a unified formulation of Schottky barrier height, transfer length, and contact resistance. Our model explains recent experiments on carbon nanotubes and 2D materials, clarifying the fundamental criteria for achieving scalable, low-resistance contacts.

Metal contacts to semiconductors must exhibit low resistance at short contact lengths for nanoscale electronics [1]. Since contact resistance increases exponentially with the Schottky barrier height Φ_B , understanding and predicting Φ_B is central to contact physics. In the Schottky-Mott limit, the n -type barrier height is $\Phi_{Bn} = W_M - \chi_S$, where W_M is the metal workfunction and χ_S is the semiconductor electron affinity [2, 3]. This yields a pinning factor $S_p = \partial\Phi_{Bn}/\partial W_M = 1$ and implies full tunability of Φ_B by varying W_M [4].

In practice, this limit is not attained due to Fermi-level pinning (FLP), where $S_p < 1$ and Φ_B becomes insensitive to W_M . While FLP in conventional semiconductors is attributed to defect-induced gap states (DIGS) arising from dangling bonds of the semiconductor surface [5–7], experiments [8–10] and density-functional theory (DFT) simulations [11–14] show that strong FLP occurs even in defect-free low-dimensional semiconductors [15]. This behavior is attributed to metal-induced gap states (MIGS), for which a comprehensive, predictive formalism has yet to be established [4].

In this Letter, we present a unified theory of MIGS and FLP in any dimension, reducing the determination of key observables— Φ_B , transfer length, and contact resistance—to analytical equations in terms of fundamental material parameters. While applicable to arbitrary band structures, in the effective-mass approximation our method reveals a universal scaling law $\Delta^{n/2-2}$ for MIGS density, where Δ is the energy depth into the gap and n is the dimensionality. Our model yields transparent interpretations of experimental results for carbon nanotube (CNT) and transition-metal dichalcogenide (TMD) contacts and provides a tractable alternative to numerical ‘black-box’ simulations. This work thus offers a clearer understanding of contact physics, the associated trade-offs, and pathways to scalable, low-resistance interfaces.

Analytical model of contact physics—Let M, S , and X denote the metal, semiconductor away from contact, and semiconductor-under-metal regions, respectively (Fig. 1(a)), with corresponding densities of states (DoS) $\rho_{M,S,X}(E)$. Assuming a weak metal-semiconductor coupling characteristic of van der Waals interfaces [16, 17], an electron of energy E tunnels from X to M with rate

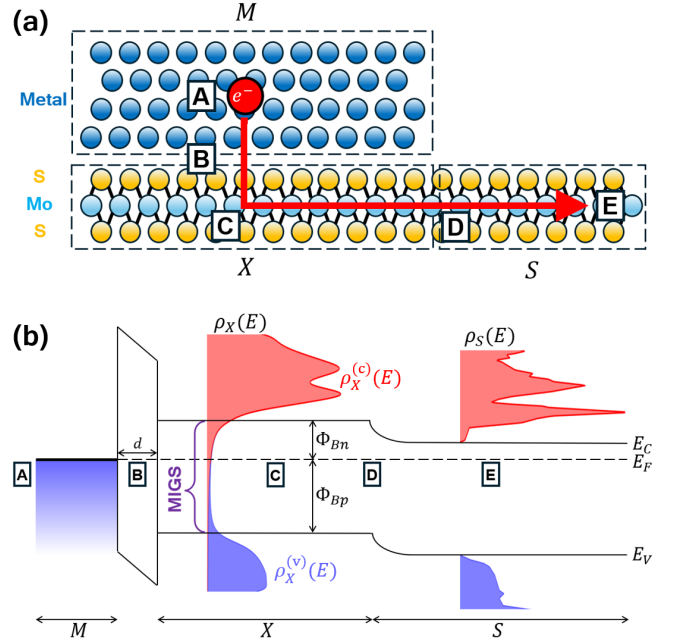


FIG. 1. Schematic of a metal-on-TMD contact (M : metal, S : semiconductor, X : semiconductor-under-metal). Based on a figure from [14]. (a) Carriers follow the injection path A-B-C-D-E. (b) Energy band diagram along the injection path. The metal-semiconductor gap has thickness d . MIGS with density $\rho_X(E)$ arise in the bandgap, comprised of conduction- ($\rho_X^{(c)}$, red) and valence- ($\rho_X^{(v)}$, blue) band contributions. n - and p -type Schottky barrier heights are Φ_{Bn} , Φ_{Bp} .

$\Gamma(E)/\hbar$ given by Fermi’s Golden Rule [18–20]:

$$\Gamma(E) = 2\pi|t|^2\rho_M(E). \quad (1)$$

t is the Hamiltonian matrix element between the wavefunctions of M and X , which is approximately energy-independent [18]. Since the electron has a finite lifetime $\hbar/\Gamma(E)$, its energy level broadens into a Lorentzian lineshape [21–23]. Every electron in X experiences a similar interaction, so $\rho_X(E)$ is obtained by convolving $\rho_S(E)$ with a Lorentzian kernel of width $\Gamma(E)$:

$$\rho_X(E) = \int_{-\infty}^{\infty} \frac{\Gamma(E)/\pi}{(E' - E)^2 + |\Gamma(E)|^2} \rho_S(E') dE'. \quad (2)$$

MIGS density is defined as $\rho_X(E)$ in the bandgap. Thus,

MIGS are Lorentzian tail states of the semiconductor bands resulting from energy broadening (Fig. 1(b)), and can be split into conduction- and valence-band contributions since $\rho_S(E)$ is nonzero only in the bands:

$$\rho_X(E) = \rho_X^{(c)}(E) + \rho_X^{(v)}(E). \quad (3)$$

Deep in the bandgap ($\Delta \gg \Gamma$), $\rho_X^{(c,v)}(E)$ scales with the energy depth Δ from its respective band edge as

$$\rho_X^{(c,v)}(E) \propto \Gamma(E) m_{\text{eff}}^{n/2} \Delta^{n/2-2} \quad (4)$$

for an n -dimensional semiconductor with effective mass m_{eff} . We derive this scaling law and give exact formulas for $\rho_X^{(c,v)}(E)$ in Appendix A. For a given coupling Γ , Eq. (4) suggests that lower-dimensional materials may exhibit inherently weaker FLP because their DoS provides fewer states to redistribute into the gap. Thus, MIGS is lowest in 1D (CNTs), followed by 2D (TMDs), and then 3D (Fig. A1).

With $\rho_X(E)$ established, we incorporate it into the Cowley-Sze framework [6] to predict the Schottky barrier height at the M - X interface. Following Vázquez *et al.* [21], the charge neutrality level (CNL) of X follows by requiring its total electron density to equal that of S :

$$\int_{-\infty}^{\text{CNL}} \rho_X(E) dE = \int_{-\infty}^{E_V} \rho_S(E) dE. \quad (5)$$

We discuss the relation between this definition of CNL and Tersoff's classic definition [7] in Appendix B. In equilibrium, the net charge density on X resulting from the displacement of the Fermi level E_F from CNL is balanced by opposite charge on the metal surface. Cowley and Sze's model [6] yields

$$\chi_S - W_M = E_F - E_C + \frac{q^2 d}{\epsilon} \int_{\text{CNL}}^{E_F} \rho_X(E) dE. \quad (6)$$

The Schottky barrier heights are $\Phi_{Bn} = E_C - E_F$ and $\Phi_{Bp} = E_F - E_V$.

Macroscopic transport properties are obtained via thermal averages at the Fermi surface. The specific contact resistivity ρ_C , quantum resistance R_Q , and sheet resistance R_{sh} of the M - X interface are given by [26]

$$\rho_C^{-1} = \frac{\pi q^2}{h} \int dE \left(-\frac{\partial f_0}{\partial E} \right) \Gamma(E) \rho_X(E) \quad (7)$$

$$R_Q^{-1} = \frac{2q^2}{h} \int dE \left(-\frac{\partial f_0}{\partial E} \right) M(E) \quad (8)$$

$$R_{\text{sh}}^{-1} = \frac{2q^2}{h} \int dE \left(-\frac{\partial f_0}{\partial E} \right) M_{2\text{D}}(E) \lambda(E) \quad (9)$$

where $f_0(E) = \frac{1}{\exp\left(\frac{E-E_F}{kT}\right)+1}$ is the Fermi-Dirac function, $M(E)$ is the number of transport modes in the semiconductor at energy E , $M_{2\text{D}}(E)$ is the mode density per

unit width, and $\lambda(E)$ is the mean free path for backscattering in X . The exponential dependence of contact resistance on barrier height, $R_Q \propto \exp(\Phi_B/kT)$, emerges from Eq. (8) and reflects thermal emission over the Schottky barrier.

Finally, these transport properties can be used to compute the transfer length L_t and contact resistance R_C at contact length L_C . We use the model of Solomon [27], repeated here for convenience, which generalizes the transmission-line model [28] to ballistic (e.g., CNT) and diffusive (e.g., TMD) transport under the contact:

$$L_t = \frac{1}{\sqrt{2\alpha\beta + \beta^2}} \quad (10)$$

$$R_C = \frac{R_Q}{2\beta L_t} \coth\left(\frac{L_C}{L_t}\right) \quad (11)$$

where $\alpha = \frac{R_{\text{sh}}}{R_Q}$ and $\beta = \frac{R_Q}{2\rho_C}$. Eq. (10) yields scaling laws for L_t in terms of Γ and other variables. Using $\langle \rangle$ to denote a thermal average, we find

$$L_t \sim \frac{v_{\text{th}}}{\langle \Gamma \rangle / \hbar} \quad (12)$$

in the ballistic limit $\langle \lambda \rangle \gg \hbar v_{\text{th}} / \langle \Gamma \rangle$, and

$$L_t \sim \sqrt{\frac{v_{\text{th}} \langle \lambda \rangle}{\langle \Gamma \rangle / \hbar}} \quad (13)$$

in the diffusive limit $\langle \lambda \rangle \ll \hbar v_{\text{th}} / \langle \Gamma \rangle$, where v_{th} is the thermal velocity. Eq. (13) is equivalent to the standard result $L_t = \sqrt{\rho_C / R_{\text{sh}}}$ [28]. These scaling laws yield estimates of the interaction strength $\langle \Gamma \rangle$ from experimental values of L_t , regardless of the Schottky barrier height.

This model constitutes a complete and unified description of MIGS (Eqs. (2) and (3)), band alignment (Eqs. (5) and (6)), charge injection (Eqs. (7) to (9)), transfer length (Eqs. (10), (12) and (13)), and overall contact resistance (Eq. (11)) in low-dimensional contacts.

Benchmarking against NEGF—We validate our analytical model via direct comparison (Fig. 2) with NEGF simulations of a Pd-on-CNT contact by Su *et al.* [24], who used a coupled mode-space NEGF solver with $k \cdot p$ Hamiltonian. To ensure direct comparison, we adopt their assumptions: (1) (13,0)-chirality CNT (2) wide-band metal, or $\Gamma(E) = \text{const.}$ [25] (3) p -type contact with zero Schottky barrier, inspired by low Φ_{Bp} observed in Pd-on-CNT experiments [29].

The benchmarking results confirm the model's validity in two key ways. First, the nearly exact matching of MIGS density in Fig. 2(a) validates our treatment of MIGS as Lorentzian tail states and supports the $\Delta^{-3/2}$ scaling law (Eq. (4)) for 1D materials. Second, the excellent agreement for $R_C(L_C)$ in Fig. 2(b) verifies our model for R_C and L_t as a function of L_C and Γ , confirming that stronger coupling enables shorter contacts.

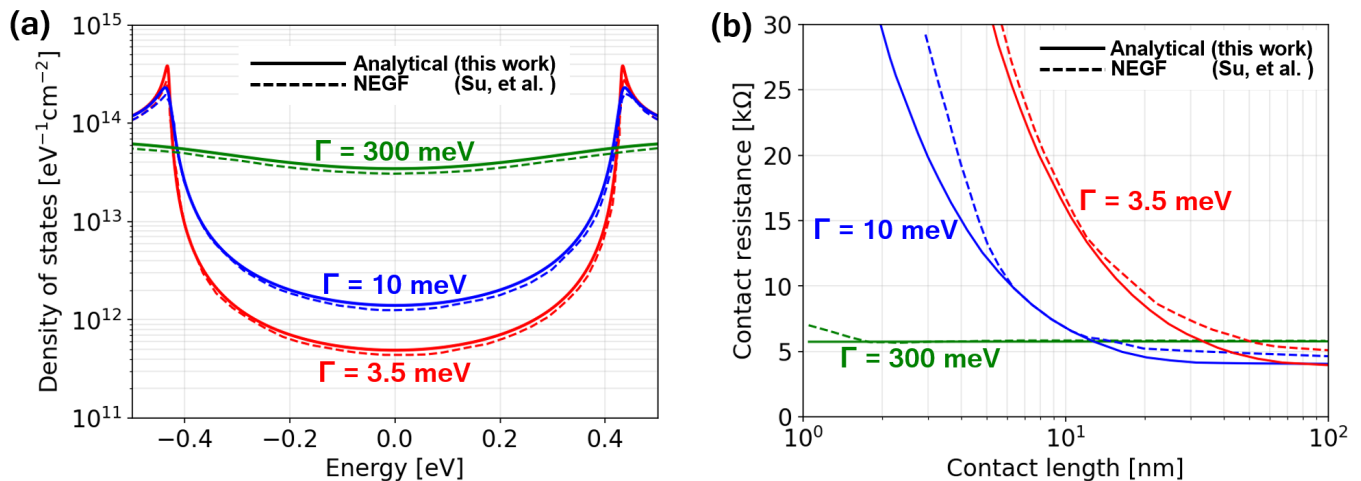


FIG. 2. Validation of our analytical model against NEGF simulations by Su *et al.* [24]. Analytical results (solid lines) show excellent agreement with NEGF results (dashed lines) across both MIGS density and length-dependence of contact resistance, $R_C(L_C)$. (a) MIGS density for Pd contact to (13,0) CNT, at various coupling strengths Γ . The metal is assumed to be wideband [25], so $\Gamma(E) = \text{const.}$ van Hove singularities are visible at $E = \pm 0.43$ eV. (b) Contact resistance as a function of contact length and coupling Γ for p -type contact, assuming $\Phi_{B_p} = 0$ for Pd-on-CNT as in [24].

Although this comparison assumes a wideband metal, our analytical framework remains valid for more realistic $\Gamma(E)$ that violates the wideband assumption (Appendix A).

Generalizability and implications—Since the bandgap and electron affinity of CNTs are determined by their chirality, Φ_B exhibits a corresponding chirality dependence. Using material parameters obtained from *ab initio* literature, our model predicts a “pinning factor” of $\partial\Phi_{B_p}/\partial d_{\text{CNT}} \approx -0.4$ eV/nm for Pd-on-CNT contacts, where d_{CNT} is the CNT diameter. This result is in excellent agreement with the DFT study of Tang *et al.* [30], showing that our analytical framework captures the chirality dependence of metal-on-CNT contacts without adjustable fitting parameters. Details are provided in the Supplemental Material [31].

Beyond 1D nanotubes, our framework provides a physical basis for the FLP observed in 2D TMDs [9, 11, 32] and explains that the shape of the MIGS density is key to the de-pinning of semimetal-on-TMD contacts [33, 34] because it shifts the CNL. Because TMD surfaces are often inherently defective, DIGS also contribute to FLP. We incorporate DIGS in our model by utilizing a semiconductor DoS $\rho_S(E)$ featuring defect-related peaks in the bandgap. Studies of metal- and semimetal-on-TMD contacts are detailed in the Supplemental Material [31].

Although we focused on 1D and 2D contacts, this model could be extended to conventional 3D contacts by accounting for the spatial decay of coupling into the bulk. In 3D, the Hamiltonian element $t(z) \propto e^{-\kappa z}$ [35, 36] introduces a depth-dependent broadening $\Gamma(E, z)$, while the presence of dangling bonds (i.e., DIGS) implies substantial surface states $\rho_S(E, z = 0)$ in the bandgap.

In summary, this Letter establishes a unified analytical framework for contacts in any dimension. Identifying MIGS as Lorentzian tail states of the semiconductor, we provide a transparent physical basis for FLP in low-dimensional interfaces, accurately reproducing rigorous simulation results without adjustable parameters. Our model uncovers the precise dependence of contact resistance on material parameters such as interface coupling, defectivity, dimensionality, and effective mass, offering a rigorous foundation for understanding and overcoming the contact bottleneck in low-dimensional electronics.

Acknowledgements—We thank Gregory Pitner and Jack Evans for useful discussions. This work is supported in part by the Department of Defense, the Microelectronics Commons, the California-Pacific-Northwest AI Hardware Hub, and member companies of the Stanford SystemX Alliance.

* jimmyqin@stanford.edu

- [1] S.-K. Su, E. Chen, T. Y. T. Hung, M.-Z. Li, G. Pitner, C.-C. Cheng, H. Wang, J. Cai, H.-S. P. Wong, and I. P. Radu, Perspective on Low-dimensional Channel Materials for Extremely Scaled CMOS, in *2022 IEEE Symposium on VLSI Technology and Circuits (VLSI Technology and Circuits)* (IEEE, Honolulu, HI, USA, 2022) pp. 403–404.
- [2] W. Schottky, Zur Halbleitertheorie der Sperrschicht- und Spitzengleichrichter, *Zeitschrift für Physik* **113**, 367 (1939).
- [3] N. Mott, The theory of crystal rectifiers, *Proceedings of the Royal Society of London. Series A. Mathematical and Physical Sciences* **171**, 27 (1939).

- [4] R. T. Tung, The physics and chemistry of the Schottky barrier height, *Applied Physics Reviews* **1**, 011304 (2014).
- [5] J. Bardeen, Surface States and Rectification at a Metal Semi-Conductor Contact, *Physical Review* **71**, 717 (1947).
- [6] A. M. Cowley and S. M. Sze, Surface States and Barrier Height of Metal-Semiconductor Systems, *Journal of Applied Physics* **36**, 3212 (1965).
- [7] J. Tersoff, Schottky Barrier Heights and the Continuum of Gap States, *Physical Review Letters* **52**, 465 (1984).
- [8] K. Sotthewes, R. Van Bremen, E. Dollekamp, T. Boulogne, K. Nowakowski, D. Kas, H. J. W. Zandvliet, and P. Bampoulis, Universal Fermi-Level Pinning in Transition-Metal Dichalcogenides, *The Journal of Physical Chemistry C* **123**, 5411 (2019).
- [9] C. Kim, I. Moon, D. Lee, M. S. Choi, F. Ahmed, S. Nam, Y. Cho, H.-J. Shin, S. Park, and W. J. Yoo, Fermi Level Pinning at Electrical Metal Contacts of Monolayer Molybdenum Dichalcogenides, *ACS Nano* **11**, 1588 (2017).
- [10] X. Wang, Y. Hu, S. Y. Kim, R. Addou, K. Cho, and R. M. Wallace, Origins of Fermi Level Pinning for Ni and Ag Metal Contacts on Tungsten Dichalcogenides, *ACS Nano* **17**, 20353 (2023).
- [11] C. Gong, L. Colombo, R. M. Wallace, and K. Cho, The Unusual Mechanism of Partial Fermi Level Pinning at Metal–MoS₂ Interfaces, *Nano Letters* **14**, 1714 (2014).
- [12] A. Fediai, D. A. Ryndyk, G. Seifert, S. Mothes, M. Claus, M. Schröter, and G. Cuniberti, Towards an optimal contact metal for CNTFETs, *Nanoscale* **8**, 10240 (2016).
- [13] Y. Guo and J. Robertson, Schottky barrier heights and band alignments in transition metal dichalcogenides, *Microelectronic Engineering* **147**, 184 (2015).
- [14] J. Kang, W. Liu, D. Sarkar, D. Jena, and K. Banerjee, Computational Study of Metal Contacts to Monolayer Transition-Metal Dichalcogenide Semiconductors, *Physical Review X* **4**, 031005 (2014).
- [15] K. S. Novoselov, A. Mishchenko, A. Carvalho, and A. H. Castro Neto, 2D materials and van der Waals heterostructures, *Science* **353**, aac9439 (2015).
- [16] M. Farmanbar and G. Brocks, First-principles study of van der Waals interactions and lattice mismatch at MoS₂ / metal interfaces, *Physical Review B* **93**, 085304 (2016).
- [17] L. Ma, Y. Wang, and Y. Liu, van der Waals Contact for Two-Dimensional Transition Metal Dichalcogenides, *Chemical Reviews* **124**, 2583 (2024).
- [18] J. Bardeen, Tunnelling from a Many-Particle Point of View, *Physical Review Letters* **6**, 57 (1961).
- [19] N. Nemeč, D. Tománek, and G. Cuniberti, Contact Dependence of Carrier Injection in Carbon Nanotubes: An *Ab Initio* Study, *Physical Review Letters* **96**, 10.1103/physrevlett.96.076802 (2006).
- [20] A. D. Gottlieb and L. Wesolowski, Bardeen’s tunnelling theory as applied to scanning tunnelling microscopy: a technical guide to the traditional interpretation, *Nanotechnology* **17**, R57 (2006).
- [21] H. Vázquez, R. Oszwaldowski, P. Pou, J. Ortega, R. Pérez, F. Flores, and A. Kahn, Dipole formation at metal/PTCDA interfaces: Role of the Charge Neutrality Level, *Europhysics Letters (EPL)* **65**, 802 (2004).
- [22] H. Vázquez, W. Gao, F. Flores, and A. Kahn, Energy level alignment at organic heterojunctions: Role of the charge neutrality level, *Physical Review B* **71**, 041306 (2005).
- [23] G. D. Mahan, *Many-Particle Physics* (Springer US, Boston, MA, 2000).
- [24] S.-K. Su, E. Chen, A. Sanchez-Soares, T. Kelly, G. Fagas, J. C. Greer, G. Pitner, H.-S. P. Wong, and I. P. Radu, Effect of Metal Coupling on Schottky Barrier Height Extraction, in *2023 International Conference on Simulation of Semiconductor Processes and Devices (SISPAD)* (IEEE, Kobe, Japan, 2023) pp. 109–112.
- [25] F. Covito, F. G. Eich, R. Tuovinen, M. A. Sentef, and A. Rubio, Transient Charge and Energy Flow in the Wide-Band Limit, *Journal of Chemical Theory and Computation* **14**, 2495 (2018).
- [26] M. Lundstrom and C. Jeong, *Near-Equilibrium Transport: Fundamentals and Applications*, Lessons from Nanoscience: A Lecture Notes Series, Vol. 2 (WORLD SCIENTIFIC, 2013).
- [27] P. M. Solomon, Contact Resistance to a One-Dimensional Quasi-Ballistic Nanotube/Wire, *IEEE Electron Device Letters* **32**, 246 (2011).
- [28] H. Berger, Models for contacts to planar devices, *Solid-State Electronics* **15**, 145 (1972).
- [29] G. Pitner, G. Hills, J. P. Llinas, K.-M. Persson, R. Park, J. Bokor, S. Mitra, and H.-S. P. Wong, Low-Temperature Side Contact to Carbon Nanotube Transistors: Resistance Distributions Down to 10 nm Contact Length, *Nano Letters* **19**, 1083 (2019).
- [30] Y. Tang, Y. Zhang, M. Zhu, T. Zhang, F. Zhang, L. Wang, Y. Zhao, H. Zhu, Z. Wu, F. Liu, and B. Li, Band Alignment among CNTs with Varying Diameters and Schottky Barrier Fluctuations between CNTs and Metals: A First-Principles Study, *ACS Applied Nano Materials* **8**, 8088 (2025).
- [31] See the Supplemental Material for detailed studies of CNT and TMD contacts.
- [32] X. Wang, Y. Hu, S. Y. Kim, K. Cho, and R. M. Wallace, Mechanism of Fermi Level Pinning for Metal Contacts on Molybdenum Dichalcogenide, *ACS Applied Materials & Interfaces* **16**, 13258 (2024).
- [33] P.-C. Shen, C. Su, Y. Lin, A.-S. Chou, C.-C. Cheng, J.-H. Park, M.-H. Chiu, A.-Y. Lu, H.-L. Tang, M. M. Tavakoli, G. Pitner, X. Ji, Z. Cai, N. Mao, J. Wang, V. Tung, J. Li, J. Bokor, A. Zettl, C.-I. Wu, T. Palacios, L.-J. Li, and J. Kong, Ultralow contact resistance between semimetal and monolayer semiconductors, *Nature* **593**, 211 (2021).
- [34] L. Hoang, A. I. Khan, R. K. A. Bennett, H.-m. Kim, Z. Zhang, M. Hocking, A. R. Choi, I.-K. Oh, A. J. Mannix, and E. Pop, Enabling P-type Conduction in Bilayer WS₂ with NbP Topological Semimetal Contacts (2024), arXiv:2409.18926 [cond-mat].
- [35] F. Heiman and G. Warfield, The effects of oxide traps on the MOS capacitance, *IEEE Transactions on Electron Devices* **12**, 167 (1965).
- [36] J. Lowell, Tunnelling between metals and insulators and its role in contact electrification, *Journal of Physics D: Applied Physics* **12**, 1541 (1979).
- [37] S. Datta, *Electronic Transport in Mesoscopic Systems*, 1st ed. (Cambridge University Press, 1995).
- [38] E. N. Economou, *Green’s Functions in Quantum Physics*, edited by M. Cardona, P. Fulde, K. Von Klitzing, H.-J. Queisser, R. Merlin, and H. Störmer, Springer Series in Solid-State Sciences, Vol. 7 (Springer Berlin Heidelberg, Berlin, Heidelberg, 2006).

End Matter

Appendix A: MIGS density—We derive Eq. (4) in the effective-mass approximation and provide general formulas valid anywhere in the bandgap. The DoS of the conduction band of an n -dimensional semiconductor is

$$\rho_S^{(c)}(E) = A(E - E_C)^{n/2-1} \Theta(E - E_C) \quad (\text{A1})$$

where A depends on effective mass, $A \propto m_{\text{eff}}^{n/2}$ [26]. To evaluate Eq. (2) for the conduction band, we use the Green's function formalism [23, 37]

$$\rho_X^{(c)}(E) = -\frac{1}{\pi} \text{Im}(G(z)) \quad (\text{A2})$$

with $z(E) = E - E_C + i\Gamma(E)$. The corresponding complex Green's functions in $n = 1, 2, 3$ dimensions are [38]

$$G_{1D}(z) = -A\pi/\sqrt{-z} \quad (\text{A3})$$

$$G_{2D}(z) = -A \ln(-z) \quad (\text{A4})$$

$$G_{3D}(z) = -A\pi\sqrt{-z} \quad (\text{A5})$$

Defining energy depth into the gap as $\Delta(E) = E_C - E$, Eq. (A2) returns the following exact expressions for conduction-band MIGS, which modify Eq. (A1) to account for interactions with a metal (Fig. A1):

$$\rho_{X,1D}^{(c)}(E) = A \sqrt{\frac{\sqrt{\Delta^2 + |\Gamma(E)|^2} - \Delta}{2(\Delta^2 + |\Gamma(E)|^2)}} \quad (\text{A6})$$

$$\rho_{X,2D}^{(c)}(E) = \frac{A}{\pi} \cot^{-1} \left(\frac{\Delta}{\Gamma(E)} \right) \quad (\text{A7})$$

$$\rho_{X,3D}^{(c)}(E) = A \sqrt{\frac{\sqrt{\Delta^2 + |\Gamma(E)|^2} - \Delta}{2}} \quad (\text{A8})$$

These expressions are valid even if the metal is not wide-band ($\Gamma(E) \neq \text{const}$). Deep in the bandgap $\Delta \gg \Gamma(E)$, Eqs. (A6) to (A8) simplify to

$$\rho_{X,1D}^{(c)}(E) \approx \frac{A\Gamma(E)}{2} \Delta^{-3/2} \quad (\text{A9})$$

$$\rho_{X,2D}^{(c)}(E) \approx \frac{A\Gamma(E)}{\pi} \Delta^{-1} \quad (\text{A10})$$

$$\rho_{X,3D}^{(c)}(E) \approx \frac{A\Gamma(E)}{2} \Delta^{-1/2} \quad (\text{A11})$$

which results in Eq. (4). However, for even deeper energies $\Delta \gg W$, where W is the width of the conduction band, the entire band is indistinguishable from a single energy level. The DoS then decays as a Lorentzian tail $\rho_X^{(c)} \propto \Delta^{-2}$ regardless of dimension. One may use these approximations for $\rho_X^{(c,v)}(E)$ to estimate the pinning factor S_p via the classic equation [4]

$$S_p = \left(1 + \frac{q^2 d}{\epsilon} \rho_X(E_F) \right)^{-1}. \quad (\text{A12})$$

Appendix B: Discussion of charge neutrality level—We discuss how Eq. (5), which defines CNL through explicit charge conservation, relates to Tersoff's well-known theory of CNL [7]. The latter defines CNL as the solution in E to $\text{Re } G(\mathbf{R}, E) = 0$, where $G(\mathbf{R}, E)$ is the real-space Green's function of the pristine semiconductor and the distance \mathbf{R} is large. We present an intuitive understanding of Tersoff's formulation starting with the Kramers-Krönig relation, using \mathcal{P} to denote the principal value:

$$\text{Re } G(\mathbf{R}, E) = \mathcal{P} \int_{-\infty}^{\infty} \frac{\text{Im } G(\mathbf{R}, E')}{E - E'} dE'. \quad (\text{B1})$$

Eq. (A2) yields $\text{Im } G(\mathbf{R}, E) = -\pi \rho_S(\mathbf{R}, E)$, where $\rho_S(\mathbf{R}, E)$ is the number of states at energy E whose size is at least $|\mathbf{R}|$. Since \mathbf{R} is large, $\rho_S(\mathbf{R}, E)$ selects the states of the semiconductor that dominate the gap states because they protrude the furthest at the surface, making up the dangling bonds (DIGS) and interacting strongly with the metal (MIGS). $\text{Re } G(\mathbf{R}, \text{CNL}) = 0$ becomes

$$0 = \int_{-\infty}^{\infty} \frac{\rho_S(\mathbf{R}, E')}{\text{CNL} - E'} dE'. \quad (\text{B2})$$

Since $\frac{1}{\text{CNL} - E'}$ is the integral of a Lorentzian tail with very small width $\frac{1}{(E' - E)^2}$, Eq. (B2) is equivalent to

$$\int_{-\infty}^{\text{CNL}} \rho_X(\mathbf{R}, E) dE = \int_{\text{CNL}}^{\infty} \rho_X(\mathbf{R}, E) dE \quad (\text{B3})$$

where $\rho_X(\mathbf{R}, E)$ is the result of very small, energy-independent broadening applied to $\rho_S(\mathbf{R}, E)$:

$$\rho_X(\mathbf{R}, E) = \lim_{\Gamma \rightarrow 0} \int \frac{\Gamma/\pi}{(E' - E)^2 + \Gamma^2} \rho_S(\mathbf{R}, E') dE'. \quad (\text{B4})$$

Because Eq. (5) and Eq. (B3) are equivalent, we find that Tersoff's formulation correctly enforces charge conservation under the following conditions: (1) only the longest-ranged states dominate MIGS (2) these states experience weak, energy-independent broadening. Condition (2) is a reasonable assumption for the ‘‘intrinsic’’ CNL of the semiconductor surface, since the metal is unknown.

In summary, we have shown that Tersoff's formulation of CNL is a limiting case of the broader principle of charge conservation. By formulating CNL through explicit charge conservation rather than the zero of $G(\mathbf{R}, E)$, our framework remains valid even in the presence of energy-dependent coupling, or structural disorder where the Green's function $G(\mathbf{R}, E)$ of the periodic crystal no longer accurately describes the local interface phenomena that cause FLP.

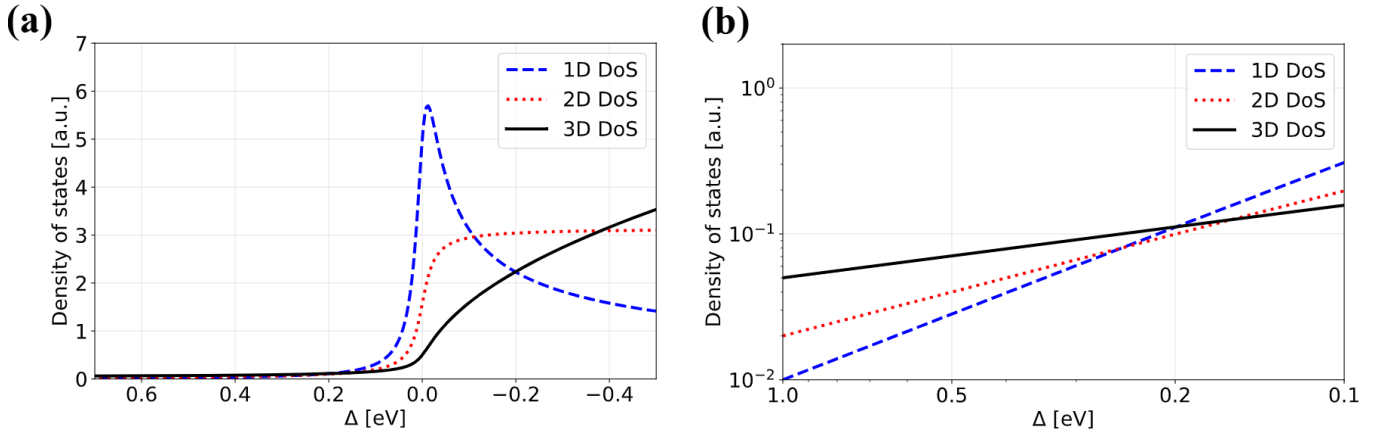


FIG. A1. Dimensional dependence of conduction-band MIGS. We show the exact MIGS density $\rho_X^{(c)}$ in $n = 1, 2, 3$ dimensions, calculated within the effective-mass approximation using Eqs. (A6) to (A8). The metal is assumed to be wideband with coupling strength $\Gamma = 20$ meV. $\Delta = E_C - E$ is the energy depth from the conduction band edge into the bandgap. (a) Linear-scale plot of the DoS. Interaction with the metal broadens the pristine band edges, giving rise to MIGS in the bandgap ($\Delta > 0$). (b) Log-log plot of MIGS density $\rho_X^{(c)}$ deep in the bandgap, demonstrating the universal $\Delta^{n/2-2}$ scaling law of Eq. (4).

Supplemental Material for
Contacts to Low-Dimensional Semiconductors:
Physical Theory and Analytical Model

Jimmy Qin and H.-S. Philip Wong
Department of Electrical Engineering,
Stanford University, Stanford, CA 94305, USA

This document provides detailed applications of our analytical theory [1] to various contacts to low-dimensional semiconductors. We provide analyses of the following topics:

- Dependence of the Schottky barrier height on the chirality of the carbon nanotube (CNT) in a metal-on-CNT contact. We use Pd-on-CNT as our case study.
- Dependence of the Schottky barrier height and pinning strength in metal-on-TMD contacts on TMD defectivity and metal-semiconductor coupling. We use Au-on-MoS₂ as our case study.
- Explanation of why semimetal-on-TMD contacts have weaker pinning than metal-on-TMD contacts. We show that the reshaped MIGS density of semimetal contacts leads to an improved pinning factor $S' = (2S + 1)/3$ compared to the pinning factor S of metal contacts with similar workfunction and coupling, which explains experimentally observed improvements in Schottky barrier height [2].

S1. METAL-ON-CNT CONTACT: Φ_B VS. CHIRALITY

Chirality describes how a graphene sheet is rolled up into a nanotube and determines CNT properties important for contact physics, such as band gap E_g , diameter d_{CNT} , and density of states (DoS) [3]. Understanding the effect of chirality on CNT contacts is important in choosing the optimal chirality for a CNT field-effect transistor due to the trade-off between low contact resistance and low device leakage [4]. In this section, we study the effect of CNT chirality on the p -type Schottky barrier Φ_{Bp} of a Pd-on-CNT contact and compare our analytical results to density-functional theory (DFT) results obtained by Tang *et al.* [5].

To compute the density of states and bandgap of the CNT, we use the standard tight-binding formalism [3] for CNTs with a carbon-carbon distance of $a = 1.42 \text{ \AA}$ and hopping energy $\gamma_0 = 2.7 \text{ eV}$, keeping only the leading-order contributions (for example, we use $E_g \propto d_{\text{CNT}}^{-1}$ and ignore the correction of order d_{CNT}^{-2}). Other quantities required for our model are obtained from theoretical or *ab initio* simulation literature, described in Table S1.

Our results are shown in Fig. S1, displaying the trend $\partial\Phi_{Bp}/\partial d_{\text{CNT}} \approx -0.4 \text{ eV/nm}$, which matches precisely with the DFT simulation results of Tang *et al.* [5]. The DFT results appear ‘noisier’ in Fig. S1 because the authors found significant dependence of χ_S on chirality even for CNTs of similar diameter. In contrast, we used an empirical formula

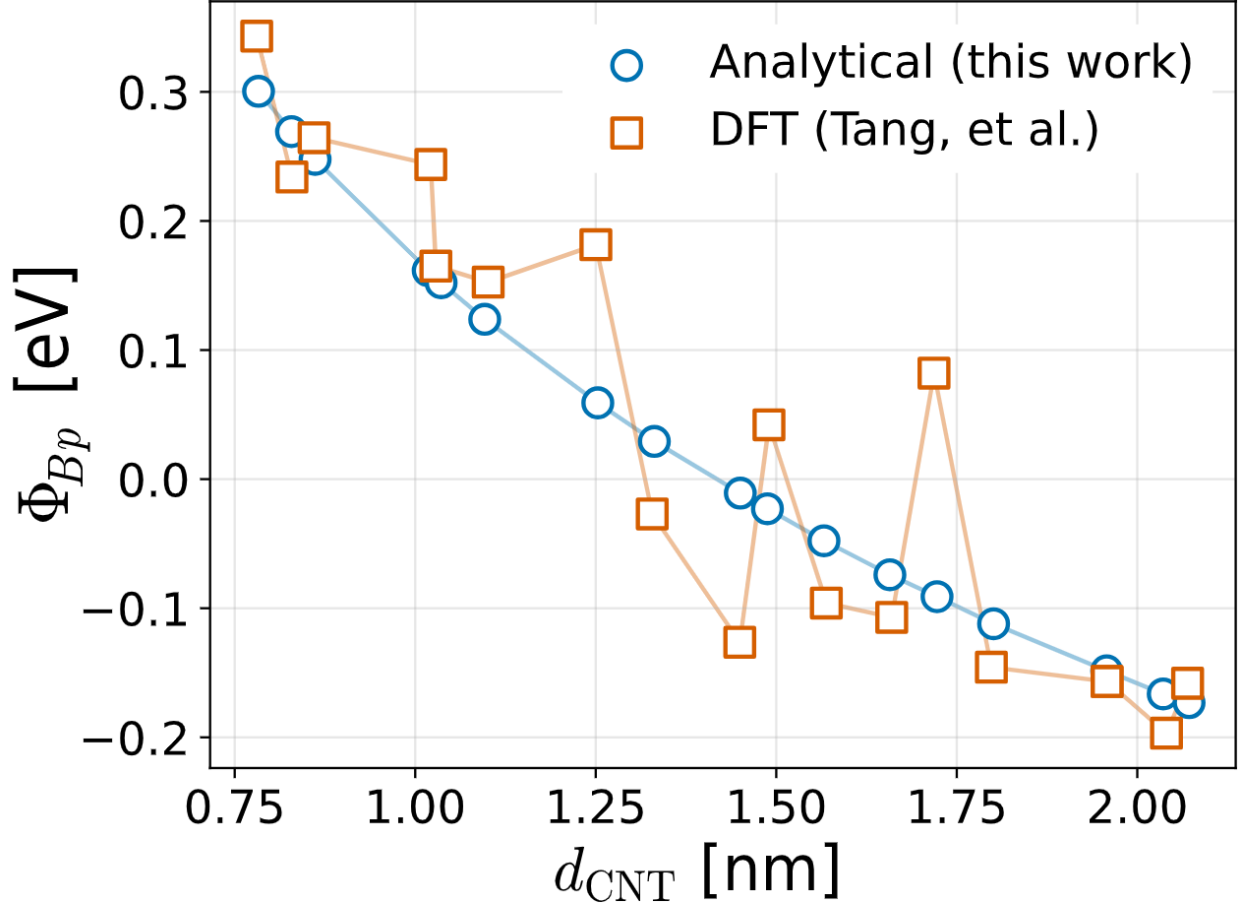


FIG. S1. Dependence of p -type Schottky barrier height Φ_{Bp} on CNT chirality for a Pd-on-CNT contact. CNT diameter d_{CNT} is a function of chirality. Each point corresponds to a CNT of different chirality (blue circles: our analytical model; orange squares: DFT simulation of Tang *et al.* [5]). Our analytical model quantitatively reproduces the trend $\partial\Phi_{Bp}/\partial d_{\text{CNT}} \approx -0.4$ eV/nm observed in the DFT simulations.

for χ_S which depends only on E_g (Table S1), which captures the primary trends of χ_S but smooths out chirality-related fluctuations. Even so, our model’s quantitative reproduction of the main trend of Φ_B suggests it is well-suited for guiding experimental device design and performing analyses without the prohibitive cost of atomistic simulations. Another advantage of our approach is the ease of investigating hypothetical scenarios. For example, if the metal-CNT interaction is weaker in reality than DFT predicts, our model provides a simple way to compute the effect of this discrepancy on contact performance.

TABLE S1. Parameters used in analytical modeling of Pd-on-CNT contacts

Quantity	Symbol	Value	Notes
Pd–CNT distance	d	3.5 Å [6]	Assuming Pd–CNT and Pd–graphene distances are similar.
Pd–CNT interaction strength	Γ	0.38 eV [7]	
Work function of Pd	W_M	5 eV [8]	
Dielectric constant of CNT	ϵ	$1 + \left(\frac{\hbar\omega_p}{5.4E_g}\right)^2$ [9]	Penn model [10] for dielectric constant. $\hbar\omega_p \approx 5$ eV is the plasma frequency along the CNT axis.
Electron affinity of CNT	χ_S	$W_M^{\text{Gr}} - \frac{E_g}{2}$ [11]	$W_M^{\text{Gr}} = 4.5$ eV is the work function of graphene.

S2. METAL-ON-TMD CONTACT: DEFECTIVITY AND PINNING

While the main text [1] and Section S1 focused on 1D CNTs, our theory is equally applicable to 2D TMDs. In metal-on-TMD contacts, Fermi-level pinning (FLP) is caused by both metal-induced gap states (MIGS) and defect-induced gap states (DIGS), due to the defectivity of the TMD [12–15]. For example, the dominant defect species in monolayer MoS₂ is the sulfur vacancy, denoted V_S, which pins the Fermi level near its trap energy, about 0.3 eV below the conduction band minimum (CBM) [14, 16].

Despite the efforts devoted to improving TMD contacts, a clear assessment of the relative contributions of MIGS and DIGS to FLP is currently lacking [17]. In this section, we demonstrate that our analytical model can fill this gap. We choose Au-on-MoS₂ for this study, since Au is a common metal for MoS₂ contacts [18]. Using parameters from experimental and *ab initio* simulation literature (Table S2), we utilize our analytical model to compute band alignment quantities—charge neutrality level CNL, Φ_{Bn} , pinning factor S_p —for wide ranges of metal-semiconductor coupling $\Gamma(E)$ and sulfur vacancy concentration $[V_S]$. For simplicity, the metal is assumed to be wideband, so $\Gamma(E) = \Gamma$ is independent of E [19].

Our results are shown in Fig. S2. The interplay between MIGS and DIGS reveals distinct regimes of pinning. In the low-coupling, low-defect limit (lower-left of Fig. S2(b,c,d)), the interface approaches the Schottky-Mott limit, where $S_p = 1$ and $\Phi_{Bn} = W_M - \chi_S$. However, the introduction of even a modest sulfur vacancy concentration ($[V_S] > 0.1\%$) rapidly shifts the CNL toward the sulfur defect peak, pinning the Schottky barrier at $\Phi_{Bn} \sim 0.3$ eV

regardless of metal coupling strength (Fig. S2(c)). In the high-coupling, low-defect limit, strong pinning occurs due to MIGS rather than DIGS (lower-right of Fig. S2(d)).

This analysis enables a quantitative understanding of the relative contributions of MIGS and DIGS in TMD contacts. To understand the contribution of MIGS, we infer Γ from experimental data using Eq. (13) in the main text, which describes how the transfer length L_t scales with Γ :

$$L_t \sim \sqrt{\frac{v_{\text{th}} \langle \lambda \rangle}{\langle \Gamma \rangle / \hbar}} \quad (\text{S1})$$

where $\langle \rangle$ denotes a thermal average. Using the values in Table S2, we find a very weak interaction strength $\langle \Gamma \rangle \approx 0.2$ meV. According to Fig. S2, $\Gamma \approx 0.2$ meV suggests that MIGS have almost no impact in Au-on-MoS₂ contacts, at least for a transfer length of $L_t = 35$ nm [18]; we conclude that the energy band alignment in Au-on-MoS₂ contacts is dominated by DIGS. This logic can be reversed: short transfer length L_t is an experimental signature of high MIGS.

To evaluate the impact of Γ on contact resistance, we consider the scaling of R_C with Γ . According to Eq. (11) of the main text [1], R_C depends on Γ as

$$R_C(\Gamma) \sim \Gamma^{-1} e^{\Phi_B(\Gamma)/kT} \quad (\text{S2})$$

where Γ^{-1} and $\Phi_B(\Gamma)$ describe the dependence of specific contact resistivity ρ_C and barrier height on Γ , respectively. Thus, Γ should be optimized to minimize ρ_C while remaining below the threshold where MIGS-induced FLP becomes significant—identified as $\Gamma \sim 3$ meV from Fig. S2. Given the estimate of $\Gamma \sim 0.2$ meV for Au-on-MoS₂ contacts, experimental efforts should *decrease defectivity* (to reduce FLP) and *increase metal coupling strength* (to reduce ρ_C). While these findings address the specific Au-MoS₂ interface, our model establishes a general framework to determine the optimal coupling for any metal-TMD combination. By integrating experimental L_t and Φ_B measurements, it provides a quantitative diagnostic to assess whether contact performance is fundamentally limited by intrinsic metal-semiconductor coupling (MIGS) or extrinsic fabrication defects (DIGS).

S3. SEMIMETAL-ON-TMD CONTACT: EXPLANATION OF DE-PINNING

Semimetal-on-TMD contacts have emerged as an effective method to reduce Φ_B and improve contact resistance R_C [27]. Our framework shows that this improvement in Φ_B is

TABLE S2. Parameters used in analytical modeling of Au-on-MoS₂ contacts

Quantity	Symbol	Value	Notes
Density of states of monolayer MoS ₂	$\rho_S(E)$	Obtained from [16]	Computed DoS in [16] covers a range of sulfur vacancy concentrations, $0 \leq [V_S] \leq 3\%$.
Workfunction of Au	W_M	5.2 eV [20]	
Electron affinity of monolayer MoS ₂	χ_S	4.2 eV [21]	
Au-MoS ₂ distance	d	3.5 Å [22]	
Dielectric constant of monolayer MoS ₂	ϵ	3 [23]	In the perpendicular direction to the MoS ₂ plane.
Transfer length of MoS ₂ contacts	L_t	35 nm [18]	
Thermal velocity	v_{th}	2×10^5 m/s	Estimated using electron effective mass of $0.35m_e$ [24].
Mean free path for backscattering in MoS ₂	λ	2 nm [25]	

not driven by a simple reduction in MIGS, but rather by an energy-dependent redistribution of MIGS that shifts the charge neutrality level (CNL) toward the relevant band edge.

According to our framework [1], the MIGS density is proportional to the coupling $\Gamma(E)$, which itself scales with the metal DoS, $\rho_M(E)$. While a standard wideband metal provides a roughly constant coupling $\Gamma(E) \approx \Gamma_0$ [19], semimetals exhibit a linear dispersion near their Dirac or Weyl points [28] and have vanishing DoS at the Fermi level E_{FM} (Fig. S3(a)). Consequently, when the semimetal E_{FM} is aligned near the semiconductor CBM E_C , the conduction-band states experience significantly less broadening compared to the valence-band states. This asymmetry causes the valence-band contribution to dominate the MIGS, effectively “pushing” the CNL toward E_C (Fig. S3(b-d)). The system Fermi level E_F is pinned close to CNL, so this CNL shift effectively de-pins E_F from the intrinsic charge neutrality level CNL_i of the semiconductor (Fig. S4).

We formalize this by deriving approximate expressions for CNL, Φ_B , and pinning factor in semimetal-on-TMD contacts. We utilize a coupling profile that accounts for the semimetal’s linear dispersion in a energy range of width W_L (Fig. S3(a)), modifying the

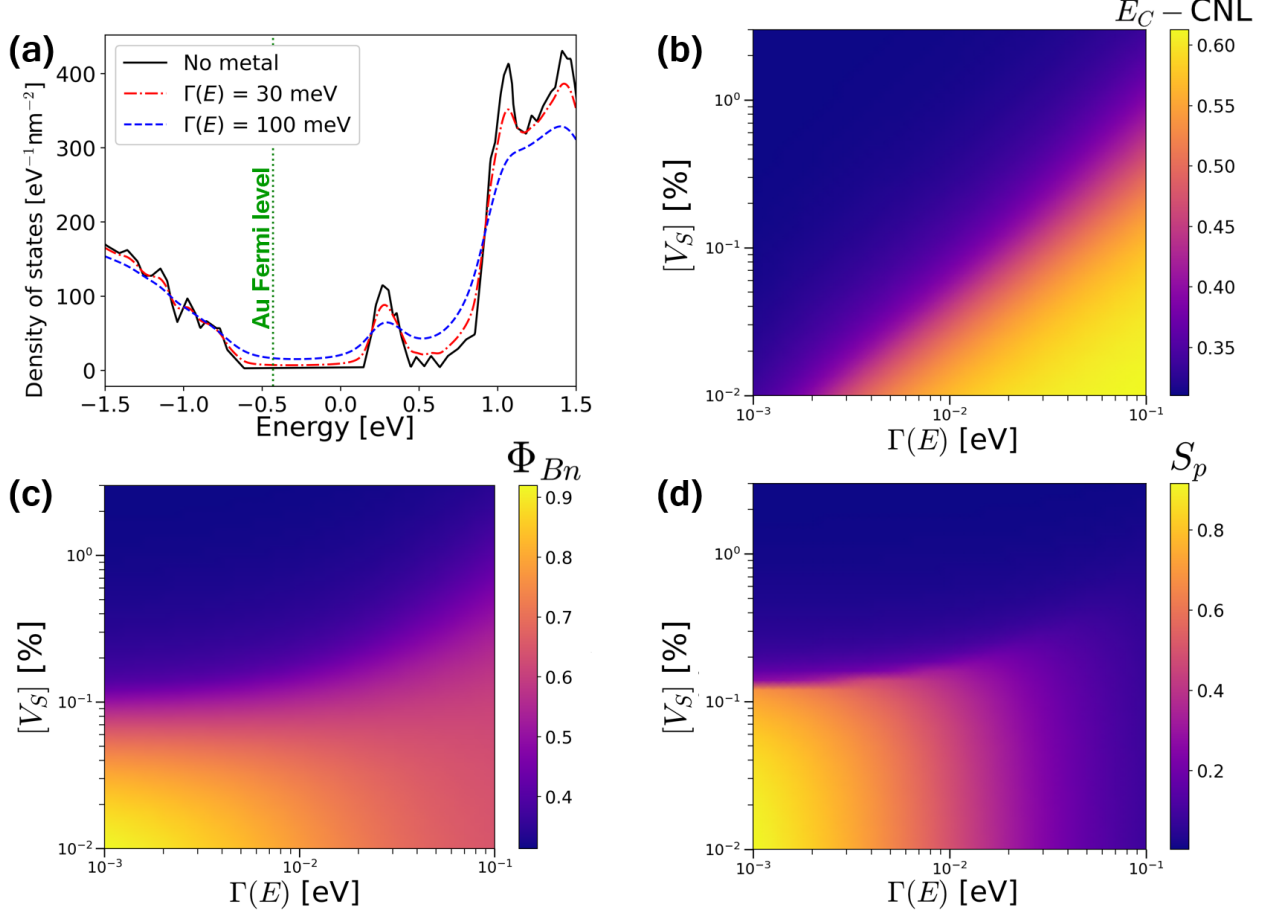


FIG. S2. Influence of metal coupling (MIGS) and defectivity (DIGS) on Au-on-MoS₂ contacts. (a) DoS of monolayer MoS₂ with $[V_S] = 3\%$ sulfur vacancy concentration and varying coupling strengths $\Gamma(E)$, from [16]. The vacancy peak is centered at $E \approx 0.3$ eV, about 0.3 eV below the CBM, and the Fermi level of Au is shown. (b) Calculated CNL relative to the CBM as a function of $\Gamma(E)$ and $[V_S]$. CNL transitions from the intrinsic limit [26] (~ 0.61 eV below CBM) to the defect-dominated limit (~ 0.31 eV below CBM). (c) n -type Schottky barrier height Φ_{Bn} , showing the transition from the Schottky-Mott limit ($\Phi_{Bn} \sim 1$ eV) to DIGS-induced pinning ($\Phi_{Bn} \sim 0.3$ eV). (d) Pinning factor $S_p = \partial\Phi_{Bn}/\partial W_M$; lower values indicate stronger pinning driven by high MIGS (right) or high DIGS (top).

wideband approximation $\Gamma(E) \approx \Gamma_0$ for a regular metal [19]:

$$\Gamma(E) = \Gamma_0 \quad \text{if } |E - E_{FM}| > W_L \quad (\text{S3})$$

$$= \Gamma_0 \frac{|E - E_{FM}|}{W_L} \quad \text{otherwise.} \quad (\text{S4})$$

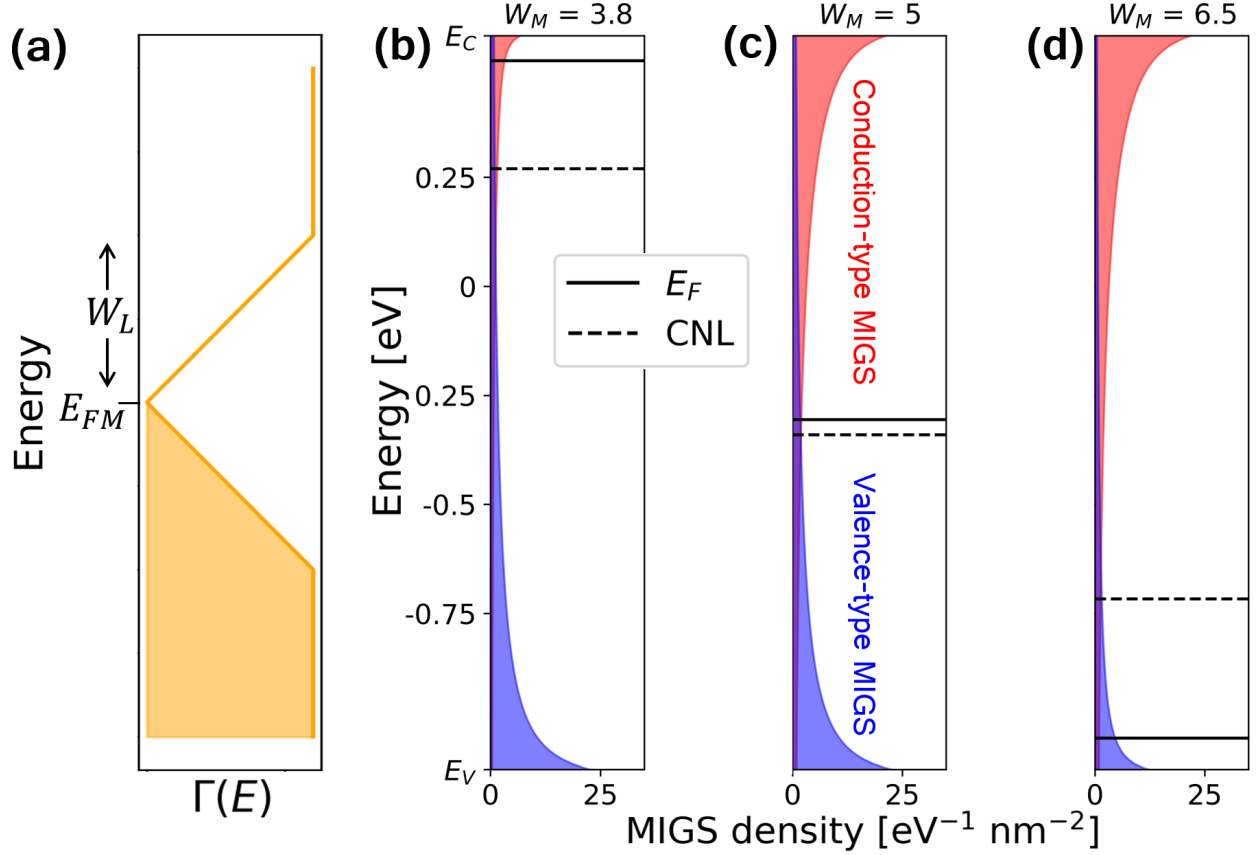


FIG. S3. Mechanism of Fermi level de-pinning in semimetal-on-TMD contacts. (a) Energy-dependent coupling strength $\Gamma(E)$ of a semimetal with linear dispersion region of width W_L centered at E_{FM} (Eq. (S3)). Orange shading indicates occupied semimetal states. (b-d) Computed MIGS density in defect-free MoS_2 for semimetal workfunctions $W_M = 3.8, 5.0,$ and 6.8 eV, respectively. Red and blue shading denote conduction- and valence-band contributions to MIGS. Dashed lines indicate CNL, while solid lines show equilibrium Fermi level E_F . Changing E_{FM} (or equivalently $W_M = E_{\text{vac}} - E_{FM}$) pulls CNL towards E_{FM} , facilitating low-barrier n -type (b) and p -type (d) contacts. These plots were generated using the full integral formalism for band alignment (see the main text [1]) rather than the analytical approximations developed in this section. The results of (b-d) confirm our analytical prediction of $\frac{d\text{CNL}}{dE_{FM}} \approx 1/3$ in the linear dispersion region.

First, we solve for the semimetal CNL relative to the wideband metal limit (CNL_i). Since MIGS is proportional to $\Gamma(E)$ (Eq. (4) in the main text [1]), we may decompose the MIGS density $\rho_X(E)$ into the product of $\Gamma(E)$ and a coupling-independent multiplier,

$$\rho_X(E) \approx \rho_{X0}(E)\Gamma(E) \quad (\text{S5})$$

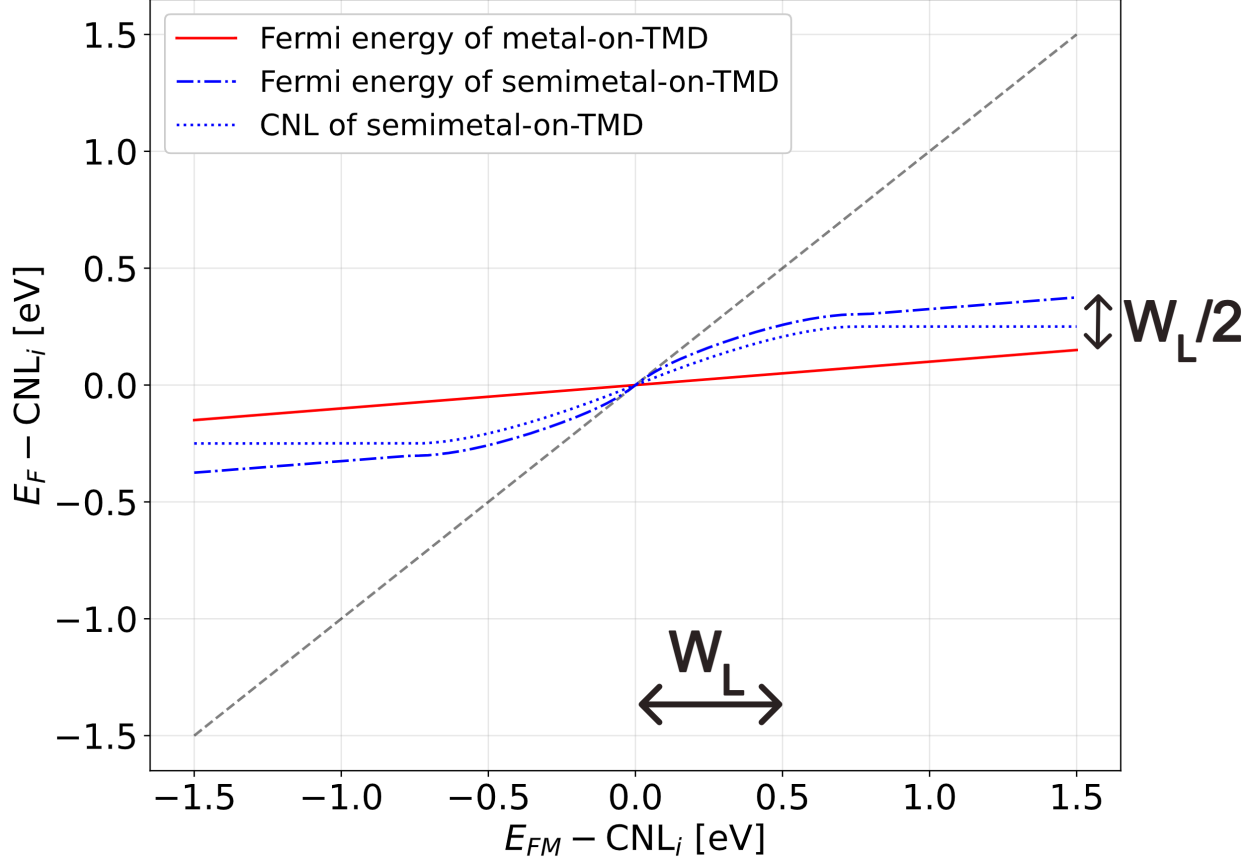


FIG. S4. Fermi level (E_F) and charge neutrality level (CNL) evolution as a function of the metal work function E_{FM} for metal and semimetal contacts. CNL_i is the charge neutrality level of the metal contact, which is independent of E_{FM} . The grey dashed line represents the unpinned Schottky-Mott limit ($S = 1$), while the red line indicates a strongly pinned metal contact ($S = 0.1$). The blue curves illustrate the de-pinning effect of a semimetal contact, where the CNL shifts in response to the semimetal work function within the linear dispersion region $|E_{FM} - CNL_i| \lesssim W_L$, where $W_L = 0.5$ eV in this case. Beyond the linear dispersion region, CNL saturates and the system reverts to standard metallic pinning behavior.

where $\rho_{X0}(E)$ is intrinsic to the semiconductor and independent of $\Gamma(E)$. The CNL definition from our main text [1] can be expressed for the metal and semimetal as

$$\begin{aligned} \int_{-\infty}^{CNL_i} \rho_{X0}(E) \Gamma_0 dE &= \int_{CNL_i}^{\infty} \rho_{X0}(E) \Gamma_0 dE \\ \int_{-\infty}^{CNL} \rho_{X0}(E) \Gamma(E) dE &= \int_{CNL}^{\infty} \rho_{X0}(E) \Gamma(E) dE \end{aligned} \quad (S6)$$

respectively. To simplify Eq. (S6) analytically, we assume that $\rho_{X0}(E)$ is approximately

constant in the bandgap, following Cowley and Sze [29]. Defining the coupling deficit $\delta\Gamma(E) = \Gamma_0 - \Gamma(E)$, Eq. (S6) yields

$$2\Gamma_0(\text{CNL} - \text{CNL}_i) + \int_{\text{CNL}}^{\infty} \delta\Gamma(E) dE - \int_{-\infty}^{\text{CNL}} \delta\Gamma(E) dE = 0 \quad (\text{S7})$$

which reduces to a quadratic equation solvable for CNL. The result is

$$\text{CNL} - \text{CNL}_i = \begin{cases} \Delta + 2W_L \cdot \text{sgn}(\Delta) \left(\sqrt{1 - \frac{|\Delta|}{2W_L}} - 1 \right) & \text{if } |\Delta| \leq 3W_L/2 \\ \frac{W_L}{2} \cdot \text{sgn}(\Delta) & \text{if } |\Delta| > 3W_L/2 \end{cases} \quad (\text{S8})$$

where $\Delta = E_{FM} - \text{CNL}_i$. Now that CNL has been established, the Fermi level E_F of the system is derived from charge balance at the semimetal-TMD interface [29]

$$\frac{q^2 d \rho_{X0}}{\epsilon} \int_{\text{CNL}}^{E_F} \Gamma(E) dE = E_{FM} - E_F \quad (\text{S9})$$

where d and ϵ are the thickness and dielectric constant of the semimetal-TMD gap. If $S = \left(1 + \frac{q^2 d \rho_{X0} \Gamma_0}{\epsilon}\right)^{-1}$ is the pinning factor for the normal metal, we find

$$E_F - \text{CNL} = \begin{cases} S\delta & \text{if } |\delta| > \frac{W_L}{1-S} \\ \delta + \text{sgn}(\delta) \left(w - \sqrt{w^2 + 2W_L|\delta| - W_L^2} \right) & \text{if } W_L < |\delta| \leq \frac{W_L}{1-S} \\ \delta + \text{sgn}(\delta) \left(w - \sqrt{\delta^2 + w^2} \right) & \text{if } |\delta| \leq W_L \end{cases} \quad (\text{S10})$$

where $\delta = E_{FM} - \text{CNL}$ and $w = \frac{SW_L}{1-S}$.

Solutions to Eqs. (S8) and (S10) are plotted in Fig. S4, revealing the intricate physics of semimetal contacts. In a standard metal contact (red line), high MIGS density pins E_F near the intrinsic CNL_i . However, a semimetal contact introduces two de-pinning mechanisms due to its linear dispersion near the Dirac or Weyl point: (1) there is no pinning at $E_{FM} = \text{CNL}_i$ because a semimetal contact has no MIGS at the Dirac or Weyl point (2) the semimetal CNL ‘‘follows’’ the semimetal Fermi energy E_{FM} (Eq. (S8)) because a shift in semimetal E_{FM} changes the shape of MIGS (Fig. S3). In contrast, a shift in E_{FM} of a normal wideband metal has no effect on MIGS since $\Gamma(E) = \text{const}$; thus, the charge neutrality level of the metal contact is fixed at CNL_i . Once $|E_{FM} - \text{CNL}_i|$ exceeds the semimetal’s linear dispersion range, the CNL saturates at $|\text{CNL} - \text{CNL}_i| = W_L/2$ because $\Gamma(E)$ becomes flat. In this regime, the linear region of the semimetal is ‘inactive’ because its energy range lies too far from CNL_i to affect the band alignment (Fig. S4).

We may further simplify Eqs. (S8) and (S10) by deriving an *effective pinning factor* $S' = \frac{dE_F}{dE_{FM}}$, averaged over the linear region $|E_{FM} - \text{CNL}_i| < 3W_L/2$ of the semimetal. The result is

$$S' \approx \frac{1 + 2S}{3} \quad (\text{S11})$$

where S is the pinning factor of a metal with similar coupling (Fig. S4). Hence, a semimetal causes the overall Fermi level E_F to move toward E_{FM} even for strongly pinned systems ($S \approx 0$), because the normal range of metal pinning factors $0 \leq S \leq 1$ corresponds to an improved range of *effective* semimetal pinning factors $\frac{1}{3} \leq S' \leq 1$. Therefore, weak FLP is caused by the shift of CNL toward E_{FM} (Eq. (S8)) rather than a true reduction in pinning strength. This CNL shift is illustrated in Fig. S3(b-d), where increasing the semimetal workfunction from 3.8 eV to 6.5 eV shifts the CNL from 0.27 eV (Fig. S3(b)) to -0.71 eV (Fig. S3(d)). The full numerical calculation of Fig. S3 thus predicts $\frac{d\text{CNL}}{dE_{FM}} \approx \frac{0.27 \text{ eV} + 0.71 \text{ eV}}{6.5 \text{ eV} - 3.8 \text{ eV}} = 0.36$, in excellent agreement with our analytical prediction of $\frac{d\text{CNL}}{dE_{FM}} \approx 1/3$ (Eq. (S8)).

In summary, we showed that semimetals effectively “bypass” FLP by changing the ratio of conduction-to-valence band MIGS, rather than by simply decreasing their density. However, the efficacy of semimetal contacts can still be compromised by chalcogen vacancies, where DIGS dominate and pin E_F to the chalcogen vacancy energy (Section S2). By deriving an *effective* pinning factor for semimetals, our model identifies a fundamental advantage: semimetal-on-TMD contacts intrinsically outperform traditional metal-on-TMD contacts of similar workfunction and coupling strength. These findings establish semimetal contacts as a uniquely effective approach to improve strongly pinned metal-semiconductor contacts.

-
- [1] See the main Letter for the full derivation and theoretical framework.
 - [2] P.-C. Shen, C. Su, Y. Lin, A.-S. Chou, C.-C. Cheng, J.-H. Park, M.-H. Chiu, A.-Y. Lu, H.-L. Tang, M. M. Tavakoli, G. Pitner, X. Ji, Z. Cai, N. Mao, J. Wang, V. Tung, J. Li, J. Bokor, A. Zettl, C.-I. Wu, T. Palacios, L.-J. Li, and J. Kong, Ultralow contact resistance between semimetal and monolayer semiconductors, *Nature* **593**, 211 (2021).
 - [3] H.-S. P. Wong and D. Akinwande, *Carbon nanotube and graphene device physics* (Cambridge university press, Cambridge (GB), 2011).
 - [4] H.-Y. Chiu, N. Safron, M. Passlack, T.-A. Chao, S.-K. Su, P.-S. Mao, C.-H. Chou, H.-Y.

- Huang, G.-Z. Wu, C.-W. Chen, C.-C. Kei, W.-H. Chang, H.-S. P. Wong, I. P. Radu, G. Pitner, and C.-H. Chien, Overcoming the Leakage and Contact Resistance Challenges in Highly Scaled PMOS and NMOS Carbon Nanotube Transistors, *Nano Letters* **25**, 3981 (2025).
- [5] Y. Tang, Y. Zhang, M. Zhu, T. Zhang, F. Zhang, L. Wang, Y. Zhao, H. Zhu, Z. Wu, F. Liu, and B. Li, Band Alignment among CNTs with Varying Diameters and Schottky Barrier Fluctuations between CNTs and Metals: A First-Principles Study, *ACS Applied Nano Materials* **8**, 8088 (2025).
- [6] M. Vanin, J. J. Mortensen, A. K. Kelkkanen, J. M. Garcia-Lastra, K. S. Thygesen, and K. W. Jacobsen, Graphene on metals: A van der Waals density functional study, *Physical Review B* **81**, 081408 (2010).
- [7] N. Nemeč, D. Tománek, and G. Cuniberti, Contact Dependence of Carrier Injection in Carbon Nanotubes: An *Ab Initio* Study, *Physical Review Letters* **96**, 10.1103/physrevlett.96.076802 (2006).
- [8] J. G. Gay, J. R. Smith, F. J. Arlinghaus, and T. W. Capelhart, Electronic structure of palladium (100), *Physical Review B* **23**, 1559 (1981).
- [9] R. Krupke, F. Hennrich, H. V. Löhneysen, and M. M. Kappes, Separation of Metallic from Semiconducting Single-Walled Carbon Nanotubes, *Science* **301**, 344 (2003).
- [10] D. R. Penn, Wave-Number-Dependent Dielectric Function of Semiconductors, *Physical Review* **128**, 2093 (1962).
- [11] A. Akturk, G. Pennington, and N. Goldsman, Quantum Modeling and Proposed Designs of CNT-Embedded Nanoscale MOSFETs, *IEEE Transactions on Electron Devices* **52**, 577 (2005).
- [12] P. Bampoulis, R. Van Bremen, Q. Yao, B. Poelsema, H. J. W. Zandvliet, and K. Sotthewes, Defect Dominated Charge Transport and Fermi Level Pinning in MoS₂ /Metal Contacts, *ACS Applied Materials & Interfaces* **9**, 19278 (2017).
- [13] S. McDonnell, R. Addou, C. Buie, R. M. Wallace, and C. L. Hinkle, Defect-Dominated Doping and Contact Resistance in MoS₂, *ACS Nano* **8**, 2880 (2014).
- [14] D. Liu, Y. Guo, L. Fang, and J. Robertson, Sulfur vacancies in monolayer MoS₂ and its electrical contacts, *Applied Physics Letters* **103**, 183113 (2013).
- [15] L. Huang, L. Tao, K. Gong, Y. Li, H. Dong, Z. Wei, and J. Li, Role of defects in enhanced Fermi level pinning at interfaces between metals and transition metal dichalcogenides, *Physical*

- Review B **96**, 205303 (2017).
- [16] S. M. Gali, A. Pershin, A. Lherbier, J.-C. Charlier, and D. Beljonne, Electronic and Transport Properties in Defective MoS₂ : Impact of Sulfur Vacancies, *The Journal of Physical Chemistry C* **124**, 15076 (2020).
- [17] X. Liu, M. S. Choi, E. Hwang, W. J. Yoo, and J. Sun, Fermi Level Pinning Dependent 2D Semiconductor Devices: Challenges and Prospects, *Advanced Materials* **34**, 2108425 (2022).
- [18] C. D. English, G. Shine, V. E. Dorgan, K. C. Saraswat, and E. Pop, Improved Contacts to MoS₂ Transistors by Ultra-High Vacuum Metal Deposition, *Nano Letters* **16**, 3824 (2016).
- [19] F. Covito, F. G. Eich, R. Tuovinen, M. A. Sentef, and A. Rubio, Transient Charge and Energy Flow in the Wide-Band Limit, *Journal of Chemical Theory and Computation* **14**, 2495 (2018).
- [20] Y. Ishida, J. K. Jung, M. S. Kim, J. Kwon, Y. S. Kim, D. Chung, I. Song, C. Kim, T. Otsu, and Y. Kobayashi, Work function seen with sub-meV precision through laser photoemission, *Communications Physics* **3**, 158 (2020).
- [21] J. Xiao, Y. Zhang, H. Chen, N. Xu, and S. Deng, Enhanced Performance of a Monolayer MoS₂/WSe₂ Heterojunction as a Photoelectrochemical Cathode, *Nano-Micro Letters* **10**, 60 (2018).
- [22] Y.-C. Huang, L.-C. He, K.-Y. Yeh, K.-B. Lin, H.-T. Liu, S.-J. Chiu, Y.-G. Lin, Y.-W. Tsai, J.-M. Lin, S.-H. Chang, T.-M. Wu, K. K.-H. Lin, S.-Y. Wang, C.-H. Chien, C.-L. Lin, S.-J. Chang, E. Y. Chang, and C. Hu, Large-Period van der Waals Epitaxy of Au on MoS₂ at Room Temperature: Moiré-Engineered Interfaces for Nanoelectronics, *ACS Applied Nano Materials* **8**, 18208 (2025).
- [23] M. Belete, S. Kataria, U. Koch, M. Kruth, C. Engelhard, J. Mayer, O. Engström, and M. C. Lemme, Dielectric Properties and Ion Transport in Layered MoS₂ Grown by Vapor-Phase Sulfurization for Potential Applications in Nanoelectronics, *ACS Applied Nano Materials* **1**, 6197 (2018).
- [24] T. Cheiwchanchamnangij and W. R. L. Lambrecht, Quasiparticle band structure calculation of monolayer, bilayer, and bulk MoS₂, *Physical Review B* **85**, 205302 (2012).
- [25] C. D. English, K. K. H. Smithe, R. L. Xu, and E. Pop, Approaching ballistic transport in monolayer MoS₂ transistors with self-aligned 10 nm top gates, in *2016 IEEE International Electron Devices Meeting (IEDM)* (IEEE, San Francisco, CA, USA, 2016) pp. 5.6.1–5.6.4.
- [26] J. Tersoff, Schottky Barrier Heights and the Continuum of Gap States, *Physical Review Letters*

- 52**, 465 (1984).
- [27] X. Liu, K. Xing, C. Sin Tang, S. Sun, P. Chen, D.-C. Qi, M. B. Breese, M. S. Fuhrer, A. T. Wee, and X. Yin, Contact resistance and interfacial engineering: Advances in high-performance 2D-TMD based devices, *Progress in Materials Science* **148**, 101390 (2025).
- [28] B. Yan and C. Felser, Topological Materials: Weyl Semimetals, *Annual Review of Condensed Matter Physics* **8**, 337 (2017).
- [29] A. M. Cowley and S. M. Sze, Surface States and Barrier Height of Metal-Semiconductor Systems, *Journal of Applied Physics* **36**, 3212 (1965).